MHD Modeling of Atmospheric Ion Escape from a Mars-like Exoplanet Orbiting TRAPPIST-1

by

Xinrun Du

Department of Physics

Bachelor of Arts

at the

University of Colorado Boulder

Committee Members

David Brain - Thesis Advisor, Outside Reader

Department of Astrophysical and Planetary Sciences

Jun Ye - Honors Council Representative

Department of Physics

Steven Pollock - Additional Committee Member

Department of Physics

Yingjuan Ma - (Ex-Officio)

Institute of Geophysics and Planetary Sciences, UCLA

November 1, 2023

Abstract

More planets are known to orbit M dwarf stars than any other type of star in our galaxy, in part because M dwarf stars are the most numerous stellar type. Habitable planets are of particular interest around these stars. However, the much closer-in habitable zone for an M dwarf creates a harsh plasma and magnetic environment for the planets, potentially causing massive atmospheric escape through various channels. An important channel for oxygen is ion escape, where charged particles are accelerated to their escape velocities. A global planetary magnetic field plays a crucial role in the interactions between stellar wind plasma and the atmosphere, but its long-assumed shielding effect on the atmosphere has been challenged in recent years, raising the question of its necessity for habitability. In this study, we explore the habitability of a Mars-like planet around the ultracool M dwarf, TRAPPIST-1, by investigating the ion escape from its atmosphere. We perform a steady-state simulation using a multispecies single-fluid magnetohydrodynamic (MHD) model with the photoionization frequency of each dominant neutral species in the Martian atmosphere and upstream stellar wind conditions at TRAPPIST-1g. In addition to unmagnetized and weakly magnetized cases, we equip Mars with a strong planetary dipole field of 5000 nT at 14 different tilt angles with respect to the +z axis to study the change in the ion loss rate. The simulation results suggest a total escape rate that is two to three orders of magnitude higher than for present-day Mars in our solar system. The magnetized cases have escape rates lower than the unmagnetized and weakly magnetized cases by a factor between 1.8 and 7.5, depending on the tilt angle. Under the maximum stellar wind condition at TRAPPIST-1g, the maximum escape rates occur at 180° and 191°, and the minimum escape rates occur at near-horizontal dipoles.

Acknowledgements

I would like to thank my advisor Yingjuan Ma for being patient, flexible, and overall a great mentor during the time I worked on this thesis and the related topics. I would also like to thank Dave for all the help in interpreting the data and producing this thesis. I am also grateful to the members of Dave's group for their constructive support. Thanks to the MACH-RHAPS team, LASP, BCM, and all my family and friends.

Table of Contents

List of Figures

Chapter 1

Introduction

As the contemporary human race proceeds in searching for a new world and other human-like life forms in the universe, it is a crucial first step to evaluate habitability based on planetary and interplanetary properties. The ability to allow the existence of liquid water and retain an atmosphere is the determining factor for surface habitability. The first condition is satisfied when a planet is at an appropriate distance from the star, and the second is fulfilled if the planet is able to withstand stellar wind erosion.

Magnetic fields are considered essential in controlling atmospheric loss. The interplanetary magnetic properties depend largely on the star and the planet-star distance. As the stellar wind carries magnetic fields of different strengths and directions, the intrinsic magnetic field configuration also varies greatly across different planets and evolves over time. Therefore, studying the change in a particular aspect of the magnetic field will aid the evaluation of habitability and give insights into the evolution of a planet.

1.1 M Dwarf Stars

Stars in the universe are created from the collapse of intra-galactic dust clouds. This process produces a hot and dense stellar core that generates nuclear fusion to balance out gravity.

The various sizes of the clouds end up in stars that burn their fuels at different rates. Bigger stars generate a much larger energy outflow (luminosity) to counteract their own weight. Therefore, smaller stars keep their cores alive by emitting low luminosity, leading to long life spans. The smallest stars on the main sequence are of spectral type M, known as M dwarf stars. These small and cool stars comprise 70% of the stellar population in the Milky Way [20]. Their abundance makes them top candidates for host stars of extrasolar habitable worlds.

Nevertheless, due to the low luminosity of M dwarf stars, the planet must be sufficiently close to the star to obtain a habitable surface temperature. Modeling results by Kopparapu et al. (2013) estimate the HZs of the main sequence stars. For an M dwarf star with a mass of 0.08 to 0.6 solar mass, the inner edge of the HZ ranges from 0.01 to 0.16 AU, and the outer edge from 0.04 to 0.25 AU [13]. The closer HZ means more exposure to potential stellar flares or Coronal Mass Ejections (CMEs). M dwarfs are found to have more frequent and intense flares [20]. These factors combined create a threatening environment for any potentially habitable rocky planet orbiting these low-mass stars.

1.2   TRAPPIST-1 System

The TRAPPIST-1 star was first discovered in 1999 and its planetary system in 2015. There is evidence for at least seven planets orbiting this ultracool M dwarf star located 39 light years away. Four of them are Earth-size and in the habitable zone. The system offers a great environment for studying potentially habitable planets around an M dwarf star in the present era and could be a target extrasolar habitat for the far future. Figure 1.1 shows the seven discovered exoplanets and the relative size of the planetary system compared to our Solar System. This study chooses the outer edge of the system's habitable zone (at the planet TRAPPIST-1g) to explore atmospheric escape.
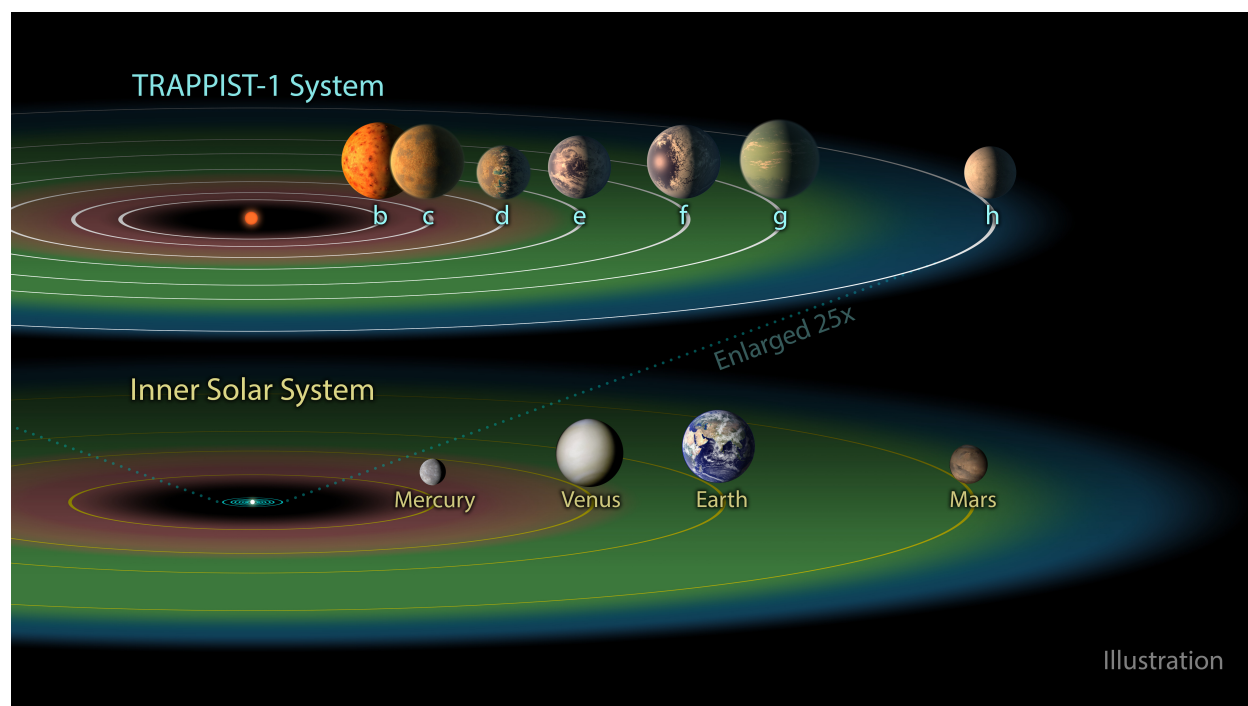
FIGURE 1.1:   TRAPPIST-1 system as compared to the Solar System.   Image link:
https://esahubble.org/images/heic1802d/.

1.3   Star-Planet Interactions

Stars emit photon radiation and stellar wind into space. The intensity of these emissions
depends on the stellar activity cycle. The stellar wind is a tenuous and fast plasma flow
ejected from the star's corona, mainly consisting of protons and electrons. The wind carries
the magnetic fields from the star, turning them into the interplanetary magnetic field (IMF).
The typical IMF is in Parker spiral configuration because of stellar rotation. The IMF is
critical in determining the space environment around a planet. The planet acts like an
obstacle to the stellar wind. If the wind is super-magnetosonic (the ratio between plasma
speed and magnetosonic wave speed is larger than 1), a bow shock would form in front of
the planet as a pressure balance between the stellar wind dynamic pressure and the thermal
pressure [6]. As a result, the stellar wind slows down abruptly and gets deflected.

Figures 1.2 and 1.3 show the magnetospheres of an unmagnetized planet and a magnetized

planet. As the stellar wind moves toward an unmagnetized planet, the typical Parker spiral
IMF field lines pile up on the dayside, drape around the conducting ionosphere of the planet,
and stretch into the nightside to form the magnetotail.
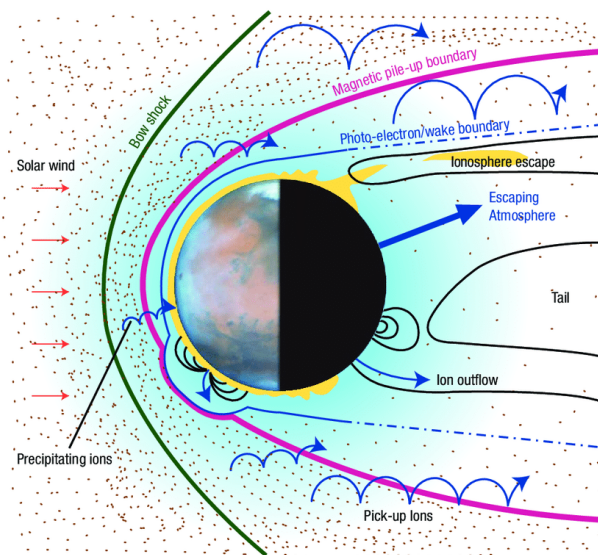
FIGURE 1.2: Induced magnetosphere of an unmagnetized planet. Adapted from [3].
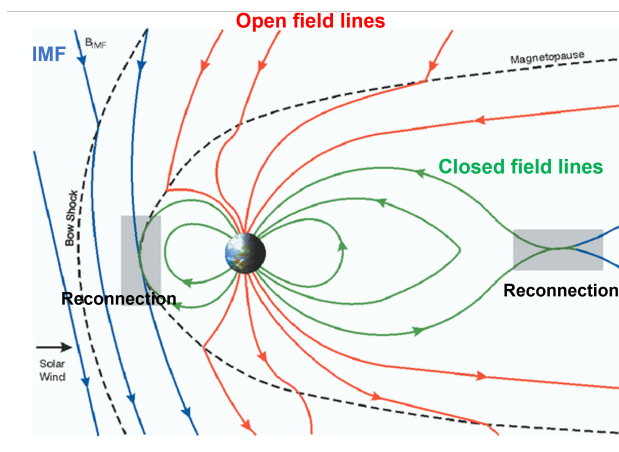
FIGURE 1.3: Intrinsic magnetosphere of a magnetized planet. Image link:
https://nap.nationalacademies.org/read/10993/chapter/4.

A magnetized planet has an intrinsic magnetic field that can be approximated as a
magnetic dipole. Because of the stellar wind pressure, this dipole appears compressed on the
dayside and stretched on the nightside. The relative orientation between field lines can cause
magnetic reconnection when they meet. Reconnection happens when two field lines break and

form two new field lines. This process changes the magnetic field geometry. Thus, it greatly impacts the ion transport and stellar wind-planet interaction in the magnetosphere. The shear angle is defined as the angle between the two types of field lines. Many reconnection events occur as antiparallel reconnections, where the shear angle is close to 180°. Other reconnections are referred to as component reconnection, where the shear angle is less than 180°. Both types of reconnection have been observed, and antiparallel reconnection occurs at a higher rate [6]. When the field lines are parallel, however, they tend to pile up without connecting.

Reconnection between IMF and the planetary magnetic field leads to three types of magnetic field line topology. The field lines with both ends connected to the planet are called closed. Open field lines have one side connected to the planet and the other to the stellar wind. Finally, the IMF has two open ends in the stellar wind. The shear angle between the geomagnetic field lines and the IMF determines whether dayside reconnection occurs, which turns closed field lines into open ones. For both unmagnetized and magnetized cases, reconnection also occurs on the nightside at the magnetotail. The field lines on the nightside point in reverse directions, introducing a current sheet where they meet at the back of the planet and causing antiparallel reconnections [6]. Different reconnection patterns lead to different magnetospheric configurations. Figure 1.4 illustrates the two types of magnetospheric configuration. For an open configuration (upper panel), the IMF and the planetary field lines are anti-parallel. Dayside reconnection happens around the substellar point, and the magnetosphere opens up for stellar wind penetration. Otherwise, the magnetosphere remains closed (lower panel) and deflects more stellar wind. The influence of reconnection on the magnetosphere results in different ion escape rates. An open configuration usually produces a higher escape rate.
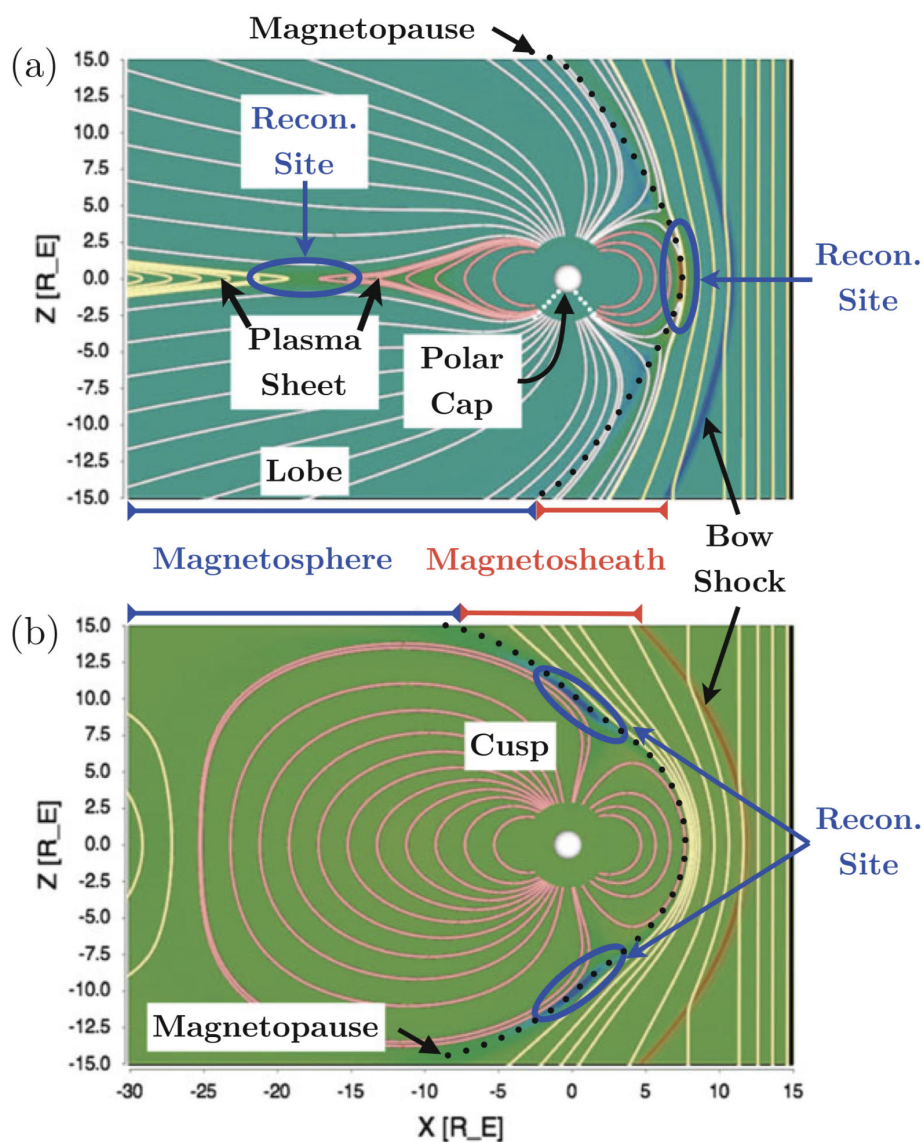
FIGURE 1.4: Open (upper panel) and closed (lower panel) magnetospheric configurations for Earth (a magnetized planet with a northward dipole), corresponding to a southward and a northward IMF, respectively. Adapted from Cassak and Fuselier (2016) [6].

1.4   Ion Escape

Atmospheric particles escape via several channels. A number of light particles leave the planet through thermal escape as they are accelerated easily to their escape velocities. Due to the larger masses, heavy atmospheric species escape the planet primarily via non-thermal

channels. Ion escape is such a channel responsible for the loss of species like oxygen. This process is summarized as ion production in the atmosphere and acceleration into the magnetosphere to overcome the planet's gravitational pull. Atmospheric particles are ionized through photoionization, charge exchange, and electron impact, with photoionization being the dominant process. Of all the stellar radiation a planet receives, extreme ultraviolet (EUV) radiation has enough energy to knock off electrons from neutrals. Ionization results in a charged region of the upper atmosphere called the ionosphere. These charged particles are accelerated by electric fields produced by the stellar wind before many of them escape to space or re-impact the ionosphere.

1.4.1   Generalized Ohm's Law

In the magnetohydrodynamic (MHD) formulation, one can obtain the generalized Ohm's law by manipulating the MHD equations with a few approximations, through which the various electric fields can be expressed as

$$\mathbf{E} = -\mathbf{u}_{sw} \times \mathbf{B} + \frac{1}{n_e e}\mathbf{J} \times \mathbf{B} - \frac{1}{n_e e}\nabla p_e + ..., \tag{1.1}$$

where $\mathbf{u}_{sw}$ is the stellar wind velocity, $\mathbf{B}$ is the magnetic field, and $\mathbf{J}$ is the current density. The three terms represent the convection field, the Hall field, and the electron pressure gradient or the ambipolar electric field, respectively [4, 19]. In a single-fluid model, however, the third term represents the thermal pressure gradient of electrons and ions together [15].

The convection field largely depends on the upstream stellar wind condition. The upstream flow has a relative velocity with the planetary ions, so it exerts a force on these stationary ions the moment they encounter each other $(= -u_{sw})$. This process is referred to as ion pickup. After the pickup, the ions move together with the stellar wind, and the effect of the convection field becomes less significant. For a typical stellar wind bulk traveling in the -x direction with an IMF dominant in the y-z direction, the convection field lies mostly in the YZ plane. In the case of radial IMF, where the IMF is aligned or anti-aligned with the stellar wind flow, the resulting $-\mathbf{u}_{sw} \times \mathbf{B}$ is small. A 2022 MAVEN observation provides

evidence for such a weak yet highly variable convection field [11]. The direction and magnitude of the convection field change as the stellar wind gets deflected past the bow shock and proceeds downstream.

$\mathbf{J} \times \mathbf{B}$ in the Hall term represents the magnetic force, which consists of magnetic tension and pressure gradient [14]. The former is proportional to field line curvature, making it a restoring force that straightens bent magnetic field lines (usually caused by IMF draping and magnetotail reconnection close to the planet). The latter points toward decreasing magnetic field strength, making it prominent further downstream. The two forces cancel out in the direction parallel to the magnetic field. Therefore, the resultant $\mathbf{J} \times \mathbf{B}$ creates an acceleration perpendicular to the magnetic field. A global MHD simulation by Lavraud et al. (2007) suggests that the two forces have comparable effects on the overall plasma acceleration [14].

An ambipolar electric field is a result of charge separation between ions and electrons in the upper atmosphere. The thermal velocity of a particle is proportional to $m^{-\frac{1}{2}}$, where m is the particle mass. As the stellar wind kinetic energy transfers to thermal energy inside the bow shock, electrons move further up in the atmosphere than ions due to the lighter mass and thus the larger thermal velocity and smaller gravitational pull. This produces an electric field that accelerates the ions upward much faster than it decelerates the electrons [2].

1.4.2   Escape from Unmagnetized and Magnetized Planets

The generalized Ohm's Law applies to both unmagnetized and magnetized planets, and the location and strength of each force are determined by the configuration of the magnetospheres. When the stellar wind encounters an unmagnetized planet, it interacts with the ionosphere directly. Planetary ions gain kinetic energy from the stellar wind and convection electric field. The energized ions gyrate along the IMF embedded in the stellar wind to leave the planet [4]. Some of them cross the field lines due to excessive energy gain or various force drifts.

A magnetized planet experiences different escape dynamics than its unmagnetized coun-

terpart. The intrinsic magnetosphere prevents the stellar wind from directly entering the ionosphere. However, the polar caps, the regions around the geomagnetic poles concentrated with open field lines, can give the stellar wind access to the ionosphere. Inside the polar caps, the ambipolar electric field is crucial to the acceleration of ions at lower altitudes, forming the "polar wind". Then, via transverse and parallel accelerations at higher altitudes, the ions escape into space along the open magnetic field lines [22]. The polar wind is known as an important ion escape channel for a magnetized planet like Earth [4].

Besides globally unmagnetized and magnetized planets, some planets have more complicated magnetic configurations. A typical example is the present-day Mars. The Mars Global Surveyor mission discovered a non-uniform and overall weak crustal field on Mars, which is thought to be the remnant of a global magnetic field in the past [1]. Although Mars is still largely unmagnetized, its crustal field adjusts the plasma boundary locations and shapes part of the magnetospheric structure, which could influence the ion escape. Based on the observations from Mars Atmosphere and Volatile Evolution (MAVEN), the crustal field both hinders and strengthens the total ion loss, leading to a minor enhancement of about 15% [10].

Although not significant, magnetotail reconnection may also contribute to the ion loss as it provides a "kick" to the plasma in the tail region. Part of magnetic energy is converted to kinetic energy as the field lines reconnect. The reconnection site acts as a dividing point. The ions on the side closer to the planet travel along the closed field lines back to the magnetic poles, hitting the atmosphere. On the other side, a small fraction of the ions are trapped along the detached field lines and pushed further into the magnetotail upon reconnection.

1.5   Modeling Ion Escape

Studies over the past two decades have developed various numerical models to simulate the process of ion escape. Ma et al. (2004) presented a high-resolution 3-D multi-species MHD model [15], which reproduced the Viking 1 observation for Mars. Another 3-D multi-species

MHD model was developed by Terada et al. (2009) [21]. Both models have been used extensively in later studies for modeling ion escape from Venus and Mars and obtained good agreement with observations. The single-fluid model was improved to multi-fluid, which separates individual ion species to obtain a different momentum for each species. One of the most updated multi-fluid MHD models is described in the Ma et al. (2019) study, which includes an additional electron pressure equation [17].

Besides treating the ions as fluids, a hybrid plasma model such as RHybrid regards the ions as macroparticle clouds to incorporate kinetic effects. While this approach more accurately tracks individual particles when at large gyroradii (compared to the planetary size), the choice of input parameters and boundary conditions is not flexible. Despite the observational and modeling efforts, the relationship between the planetary magnetic field and ion escape remains a puzzle. While a global magnetic field is assumed to protect the planet from stellar wind erosion, observational and modeling results suggest similar ion escape rates for Earth (magnetized), Venus (unmagnetized), and Mars (partially magnetized) [12]. Additional modeling work found an increase in the escape rate with the planetary dipole field strength till 10^3 nT. The escape rate starts to decrease past this value [16]. Therefore, ion escape and geomagnetic field have a more complex correlation than previously expected. Simulations usually adjust the planetary dipole strength, IMF strength, and orientation, but the dipole tilt (defined in a different plane than the IMF clock and cone angles) not common to vary planetary dipole tilt. In addition, the scenario where the IMF is radial (aligned or anti-aligned with the stellar wind flow) has not been well understood.

While the above questions remain open, models provide us with a great picture of the magnetospheric dynamics inside the Solar System. A single-fluid MHD model is known for its computational efficiency. Thus, it is an excellent tool for predicting the behavior of distant star systems, where observational data acquisition is challenging. Studies on M dwarf star systems largely rely on modeling. Nearby systems such as Proxima Centauri and TRAPPIST-1 have been targets in contemporary modeling work. Dong et al. have simulated the ion escape from Earth-like and Venus-like exoplanets orbiting M dwarf stars via single-fluid and multi-fluid MHD models [8, 9]. However, a Mars analog has yet to be investigated

as much as Venus and Earth. In this study, we explore whether a Mars-like exoplanet could be habitable at TRAPPIST-1g by investigating its atmospheric escape, and how a strong planetary dipole field with different tilt angles influences this process. Chapter 2 introduces the single-fluid multi-species MHD model used for our simulation, followed by the simulation results in Chapter 3. Chapter 4 discusses how a near-horizontal dipole is in favor of forming a closed magnetospheric structure and offers a potentially habitable environment through lower atmospheric loss.

Chapter 2

Methodology

2.1 Model Description and Simulation Set-Up

This study uses a 3-D multi-species global magnetohydrodynamic (MHD) model, where the space plasma is treated as a single perfectly conducting fluid with no charge separations and the ionosphere as a perfectly conducting sphere. The model solves a set of equations that describe the plasma behaviors, each of which is listed below:

$$\frac{\partial \rho_i}{\partial t} + \nabla \cdot (\rho_i \mathbf{u}) = S_i - L_i, \tag{2.1}$$

$$\frac{\partial (\rho \mathbf{u})}{\partial t} + \nabla \cdot \left(\rho \mathbf{u}\mathbf{u} + p\mathbf{I} + \frac{B^2}{2\mu_0}\mathbf{I} - \frac{1}{\mu_0}\mathbf{B}\mathbf{B} \right) = \rho \mathbf{G} - \rho \nu \mathbf{u} - \sum_{i=ions} L_i \mathbf{u}, \tag{2.2}$$

$$\frac{\partial}{\partial t}\left(\frac{\rho u^2}{2} + \frac{p}{\gamma - 1} + \frac{B^2}{2\mu_0} \right) + \nabla \cdot \left[\left(\frac{\rho u^2}{2} + \frac{\gamma p}{\gamma - 1} + \frac{B^2}{\mu_0} \right)\mathbf{u} - \frac{(\mathbf{B}\cdot\mathbf{u})\mathbf{B}}{\mu_0} + \mathbf{B} \times \frac{\nabla \times \mathbf{B}}{\mu_0^2 \sigma_0} \right]$$
$$= \sum_{i=ions}\sum_{n=neutrals} \frac{\rho_i \nu_{in}}{m_i + m_n}\left[3k(T_n - T_i) - m_i u^2 \right] + \rho \mathbf{u} \cdot \mathbf{G}$$
$$+ \frac{k}{\gamma - 1}\sum_{i=ions} \frac{(S_i T_n - L_i T_i)}{m_i} - \frac{1}{2}\sum_{i=ions} L_i u^2 + \frac{k}{\gamma - 1}\frac{S_e T_{n0} - L_e T_e}{m_e}$$

$$\tag{2.3}$$

$$\frac{\partial \mathbf{B}}{\partial t} + \nabla \cdot (\mathbf{u}\mathbf{B} - \mathbf{B}\mathbf{u}) = 0. \tag{2.4}$$

These equations are written in conservative form. Namely, the left side contains the time derivative of a quantity and the divergence of its flux (i.e., temporal and spatial changes), and the right side includes the source term. Equation 2.1 is a set of continuity equations for each of the four ion species (H^+, O^+, O_2^+, and CO_2^+), representing the flow of the mass. ρ_i is the mass densities for the four species ($i = 1$ to 4), and $\rho = \sum_{i=ions} \rho_i$ is the total mass density. S_i and L_i are the mass production and loss rates based on the ionization, recombination, and charge exchange between the ions and neutrals in the ionosphere. Equation 2.2 is the momentum equation for the whole plasma, where $\mathbf{G}$ counts for gravity, and ν_{in} is the ion-neutral collision frequency. The ion pressure equation, Equation 2.3, depicts the energy transfer in the system. Several parameters are contained in this equation. γ is the ratio of specific heats taken to be $\frac{5}{3}$. m_i, m_n, and m_e are masses of the ion, the neutral, and the electron, respectively, and T_i, T_n, and T_e are temperatures of the three. k is the Boltzmann constant. Finally, Equation 2.4, the magnetic induction equation, describes the evolution of the magnetic field in the conducting fluid with a velocity $\mathbf{u}$, where σ_0 is the conductivity of the ionosphere [8, 15, 17].

The above MHD equations are solved numerically via the BATS-R-US (Block Adaptive Tree Solar Wind Roe-Type Upwind Scheme) code developed by the University of Michigan. Data visualization is produced by the BATS-R-US IDL package. The simulation uses the Mars-centered stellar orbital (MSO) coordinate system, where the +x-axis points from Mars to TRAPPIST-1, the +z-axis points geographically northward, perpendicular to the Mars orbital plane, and the y-axis completes the right-handed coordinate system. The computational domain is defined by $-24R_M \leq x \leq 12R_M$ and $-16R_M \leq y, z \leq 16R_M$, where $R_M = 3,396$ km is one Mars radius. During the simulation, plasma characterized by a set of boundary conditions (density, velocity, etc.) flows in from one side and encounters the planet located inside the simulation domain, with its inner atmospheric boundary taken to be 100 km in altitude ($\approx 1.03R_M$).

The simulation uses a temporally second-order scheme with a CFL number of 0.8. Since the simulation is performed in a steady-state mode of BATS-R-US, the initial conditions and the final results are independent of physical time. The evolution of the system is instead

tracked by iteration steps. For each run, the simulation runs through 5×10^4 iteration steps, with the MHD variable data files saved every 5,000 steps. The escape rate data are saved as a separate log file every 20 steps. The simulation is stopped whenever the maximum iteration (5×10^4) is reached. A steady state is reached after around 1×10^4 steps for the cases with an unmagnetized or weakly magnetized planet, while the same occurs typically after 2 to 3×10^4 steps for the cases with a magnetized planet. Our simulation captures ten snapshots of the system, and we pick the 10th for visualization to represent a full steady state, except for one case where we pick the 8th due to saving errors of the later shots. The final escape rate for each case is calculated as the average over the last 10^4 iteration steps.

2.2 Model Input

2.2.1 Upstream Stellar Wind Conditions

For the stellar wind input, we use the upstream conditions at TRAPPIST-1g simulated by Dong et al. (2018) [8] using the Alfvén Wave Solar Model. The parameters for the stellar minimum and maximum conditions are listed in Table 2.1.

	Stellar Minimum	**Stellar Maximum**
$n\ (cm^{-3})$	205	1950
$\mathbf{u}\ (km\ s^{-1})$	$(-1032, 40, 2)$	$(-637, 40, 2)$
$T\ (10^5\ K)$	13	8.92
$\mathbf{B}_{IMF}\ (nT)$	$(-159, 20, -19)$	$(-69, 6, -28)$

TABLE 2.1: Upstream stellar wind conditions. The bold font represents a vector in the x, y, and z directions. n, $\mathbf{u}$, and T represent the stellar wind density, velocity, and temperature, respectively. $\mathbf{B}_{IMF}$ represents the IMF vector.

2.2.2 Ionization Frequencies

Unlike the present-day Mars in our solar system, a Mars-like planet at TRAPPIST-1g receives more intense EUV radiation due to the more active nature of its host star and the closer

relative distance between the two. As introduced in Chapter 1, EUV photons are responsible for ionizing neutral atmospheric particles. Hence, a higher EUV photon flux results in a higher ionization frequency, the ion production rate per neutral gas particle [19].

Each neutral species has its cross-section σ as a function of radiation wavelength λ. This quantity determines the probability that a neutral particle will be ionized upon collision with a photon. The differential ionization frequency is obtained by $\sigma(\lambda) \cdot n(\lambda)$, the product of the cross-section and the corresponding photon flux at a particular EUV wavelength, scaled to the distance of TRAPPIST-1g. With the EUV spectrum of the star, one can calculate n using the photon energy expression $E = \frac{nhc}{\lambda}$. Then, the final ionization frequency for a species is the integral of the differential ionization frequency over the EUV wavelength

$$\int_{EUV} \sigma(\lambda) \cdot n(\lambda)\ d\lambda.$$

Since CO_2 and atomic oxygen are the dominant neutral species in the Martian atmosphere, their ionization frequencies are calculated as the input parameters and listed in Table 2.2. For CO_2, we select the results for the two branches of the chemical reaction that produce major ions. The total ion production rate for each species is the product of its ionization frequency and number density as a function of altitude [19].

Neutral Species	Reaction Branch	Ionization Frequency (s^{-1})
CO_2	$CO_2 + hv \rightarrow CO_2^+ + e$	6.45×10^{-6}
	$CO_2 + hv \rightarrow CO + O^+$	1.73×10^{-7}
O	$O + hv \rightarrow O^+ + e$	1.93×10^{-6}

TABLE 2.2: Ionization frequencies for the dominant neutral species in the Martian atmosphere.

The above calculation is done through the interpolation and integration functions embedded in an IDL routine. The EUV spectrum for TRAPPIST-1 is adopted from the model results by Peacock et al. (2019) [18]. The neutral Martian atmospheric data are provided by the MACH-RHAPS center and the cross-section data on the Southwest Research Institute website: `https://phidrates.space.swri.edu`.

Planetary Magnetization	Stellar Cycle (Min/Max)	Dipole Tilt Angle (°)
Unmagnetized	Min	None
Unmagnetized	Max	None
Crustal field	Max	None
Magnetized	Max	0°, 11°,30°, 60°, 90° 120°, 150°, 180°, 191° 210°, 240°, 270°, 300°, 330°

TABLE 2.3: Simulation cases performed in this study with the selected planetary magnetization, stellar cycle condition, and the dipole tilt angle for the magnetized cases. For the magnetized case, $|\mathbf{B}_{Dipole}| = 5{,}000$ nT.

2.2.3   Simulation Cases

We perform simulation cases of different combinations of stellar wind conditions and planetary magnetic configurations to study the effect each combination has on the total ion escape rate from the planet. A specific variable of our investigation is the planetary dipole tilt angle. This angle is defined in the XZ plane as the angle between the +z axis and the dipole moment. The dipole tilt increases counterclockwise. For the cases with a magnetized planet, we use a strong dipole field of 5,000 nT, and we vary the tilt angle across the 360° circle in the plane. A total of 17 cases are run, corresponding to two unmagnetized cases with different stellar wind conditions, one case with the present-day Martian crustal field, and 14 magnetized cases, each with a different dipole tilt angle. The crustal field and the magnetized cases are investigated at the stellar maximum. The tilt angles of 11° and 191° are intended to imitate the dipole obliquity of Earth. All the cases are summarized in Table 2.3.

Chapter 3

Simulation Results

In this chapter, the simulation results of the cases listed in Chapter 2 are summarized in the following sections based on the magnetization state of the planet.

The simulation results for a Mars-like exoplanet with a crustal field are similar to the unmagnetized stellar maximum case in all aspects, with only minor differences in the total ion escape rate. The 2-D contour plots for this case are therefore not shown here. The cause for this resemblance could be the strong stellar wind and IMF compared to our Solar System, under which the effect of a relatively weak crustal field appears not significant.

3.1 Weakly and Unmagnetized Mars-like Exoplanet

Here, we compare the key features and ion escape rates for an unmagnetized Mars-like exoplanet under minimum and maximum stellar wind conditions. MHD variables are plotted as 2-D contour maps in Figures 3.2 and 3.3. The interaction patterns for the two cases appear qualitatively similar and quantitatively different.

3.1.1   System Dynamics

Stellar Wind and Magnetic Structure

Figure 3.2 shows the XZ cut of the stellar wind velocity and magnetic field around the planet. Recall that +x points from the planet to the star, and +z points northward, perpendicular to the orbital plane. The left panel depicts the bow shock location (numbered 1 in the figure). On the right panel, the IMF field lines are deflected with the stellar wind downstream from the bow shock. The relatively radial IMF here depicts a different field line pattern around the planet. For reference, Figure 3.1 shows the case where the IMF is not radial. For both cases, the field lines behind the geographic north pole warp backward and drape around the planet, forming current sheets at the reversal. This asymmetry is likely due to the difference in the direction of the wind velocity and the embedded IMF. Although the IMF also has a dominant -x component, the other two components are not negligible. When the IMF encounters the planet with anti-radial stellar wind velocity, the northern bow shock appears as a parallel shock to the IMF, and the southern shock is quasi-perpendicular. As a result, the northern shock acts like a bigger buffer to the -z pointing IMF, while the southern shock does the opposite. The field line reversal in the northern magnetotail leads to reconnection with the southern magnetotail around the $z = 0$ plane, forming another current sheet.
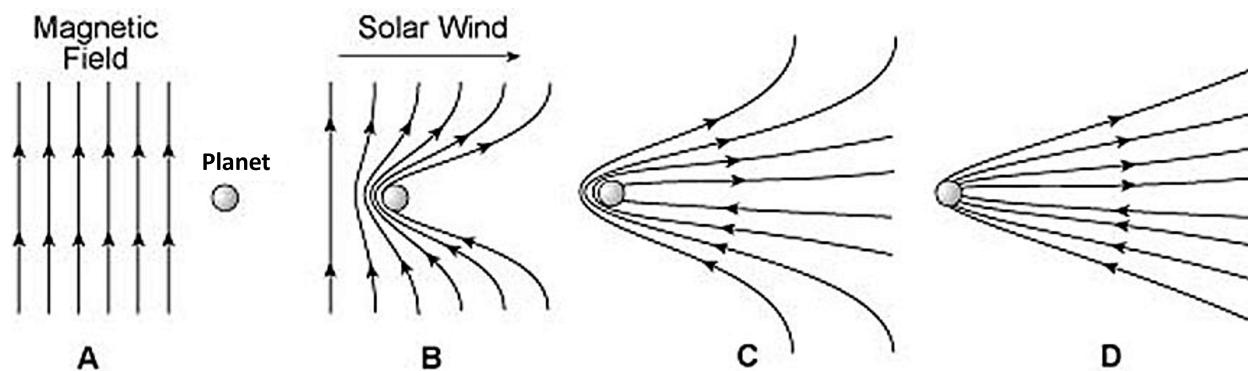

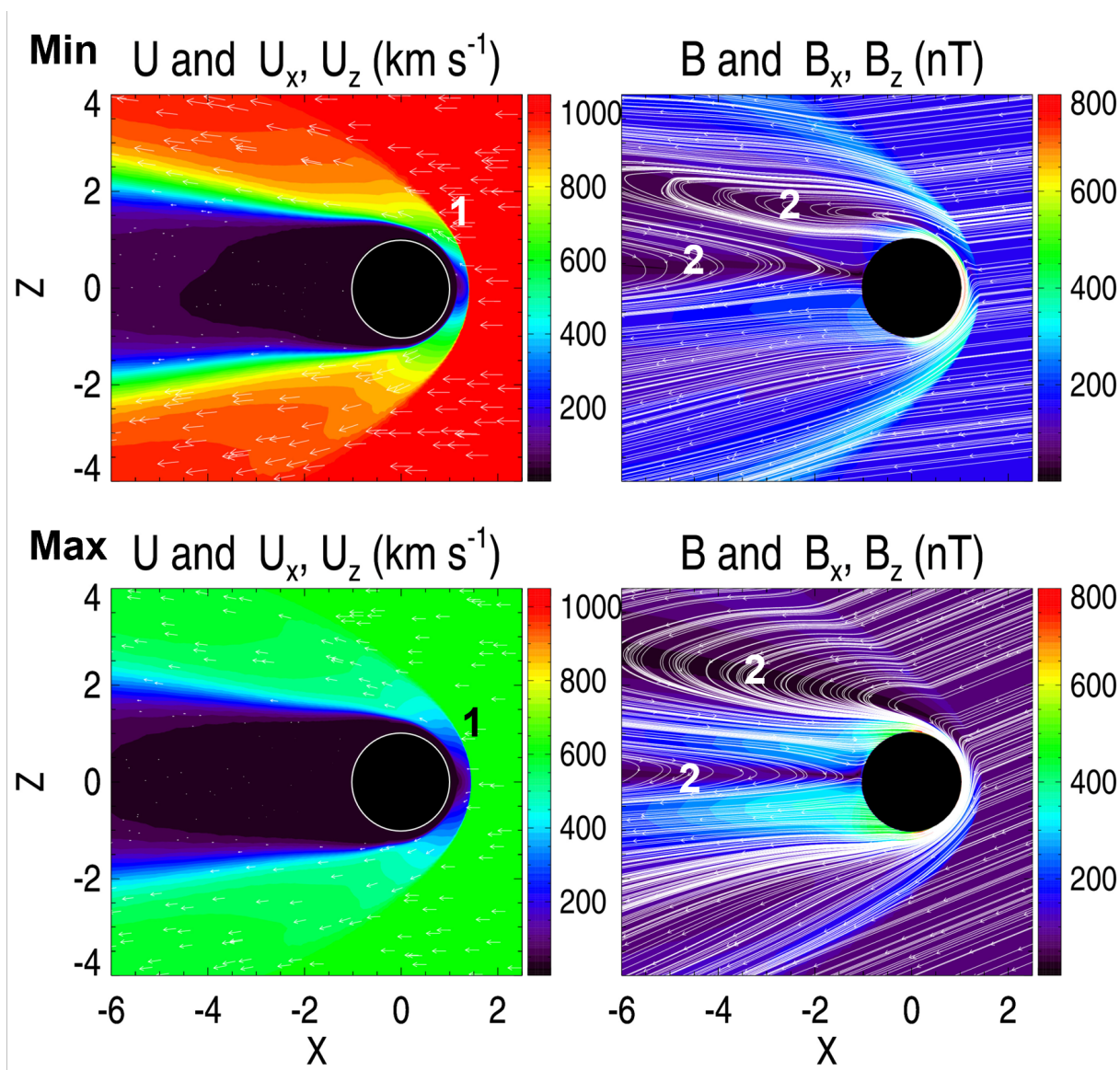FIGURE   3.1:   Non-radial   IMF   draping   around   a   planetary   body.   Image   link:
https://www.universetoday.com/tag/ionized/.

FIGURE 3.2: XZ plane cut for an unmagnetized Mars-like exoplanet at TRAPPIST-1g during the stellar minimum (upper panel) and maximum (lower panel). The contour maps show the magnitudes of the stellar wind velocity and magnetic fields. The white arrows on the left panel are the velocity vectors the plane cut. The streamlines on the right panel represent the magnetic field lines. 1 and 2 denote the bow shock and current sheet, respectively.

Ion Number Density Distribution

According to Figure 3.3, planetary ions flow away from the planet along the induced magnetotail. O^+ dominates the escape by forming a larger and denser ion cloud and higher

tail-ward flux. The density has a local maximum in the nightside current sheet, indicating that the ions are being transported to the nightside through induced magnetic field lines that converge behind the planet. This process is mainly driven by the $\mathbf{J} \times \mathbf{B}$ and pressure gradient forces, shown in Figure 3.4 in the next subsection.
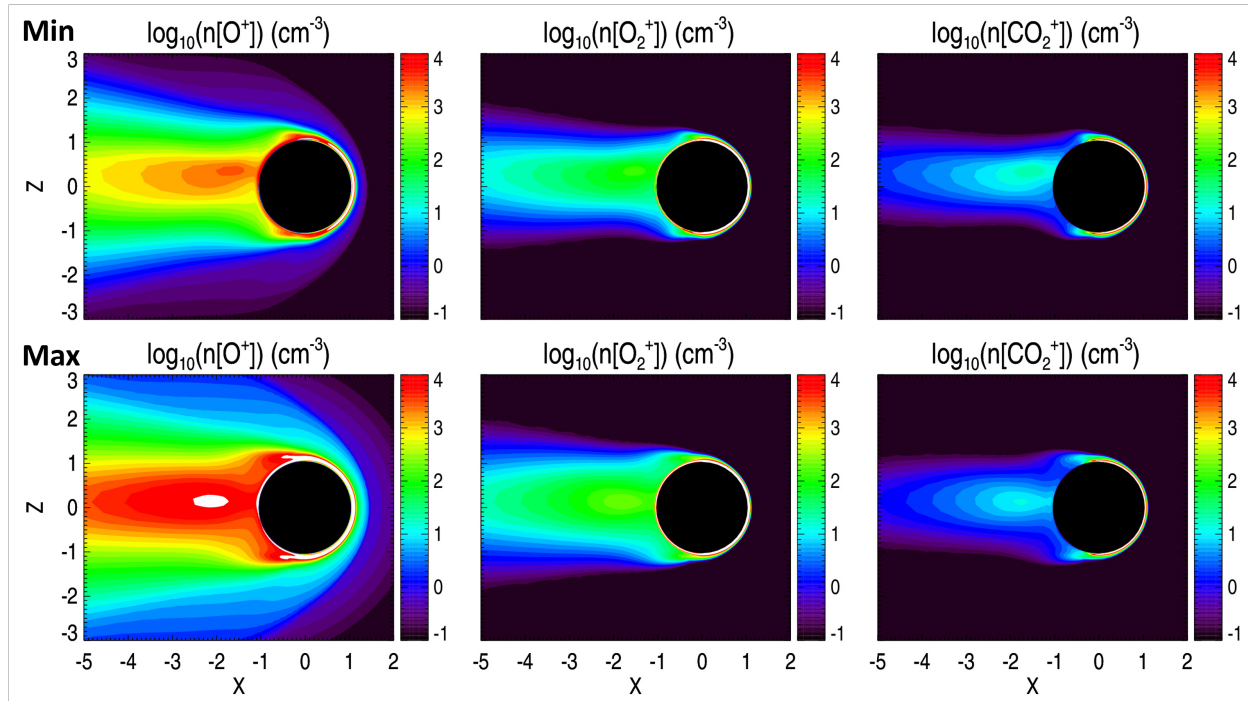

FIGURE 3.3: Ion number densities of 3 species for an unmagnetized planet in the XZ plane at the stellar minimum (upper panel) and maximum (lower panel), plotted on a log_{10} scale. The white regions on the contour map are where the density exceeds $10^4 \ cm^{-3}$.

Force Distribution

Based on the map in Figure 3.4, the unmagnetized Mars has very different $-\mathbf{u} \times \mathbf{B}$ force distributions for the two upstream stellar wind conditions. Although stellar minimum produces a stronger convection electric field, the higher total ion density at stellar maximum leads to a much larger $-\mathbf{u} \times \mathbf{B}$ force exerted on the ion during the stellar wind pickup, as shown in the first and third rows of Figure 3.4. On the dayside, $-\mathbf{u} \times \mathbf{B}$ pushes the ions to the tail region, diffuses the ion cloud, and shifts the cloud toward the +y direction by a small amount. Further away from the planet, the stellar wind and the picked-up ions move together. The effects of the $-\mathbf{u} \times \mathbf{B}$ term are less important, even though the numerical value

of $n_i q(-\mathbf{u} \times \mathbf{B})$ is large. The draped IMF creates a $\mathbf{J} \times \mathbf{B}$ force on the dayside close to the planet, which acts to oppose the stellar wind while accelerating the ions radially outward. The $\mathbf{J} \times \mathbf{B}$ force from the magnetotail current sheet points in the -x direction to pull the ions away from the planet. The stellar minimum condition induced a stronger magnetosphere to the planet. This is reflected in the wider distribution of $\mathbf{J} \times \mathbf{B}$ in the second row than in the fourth.
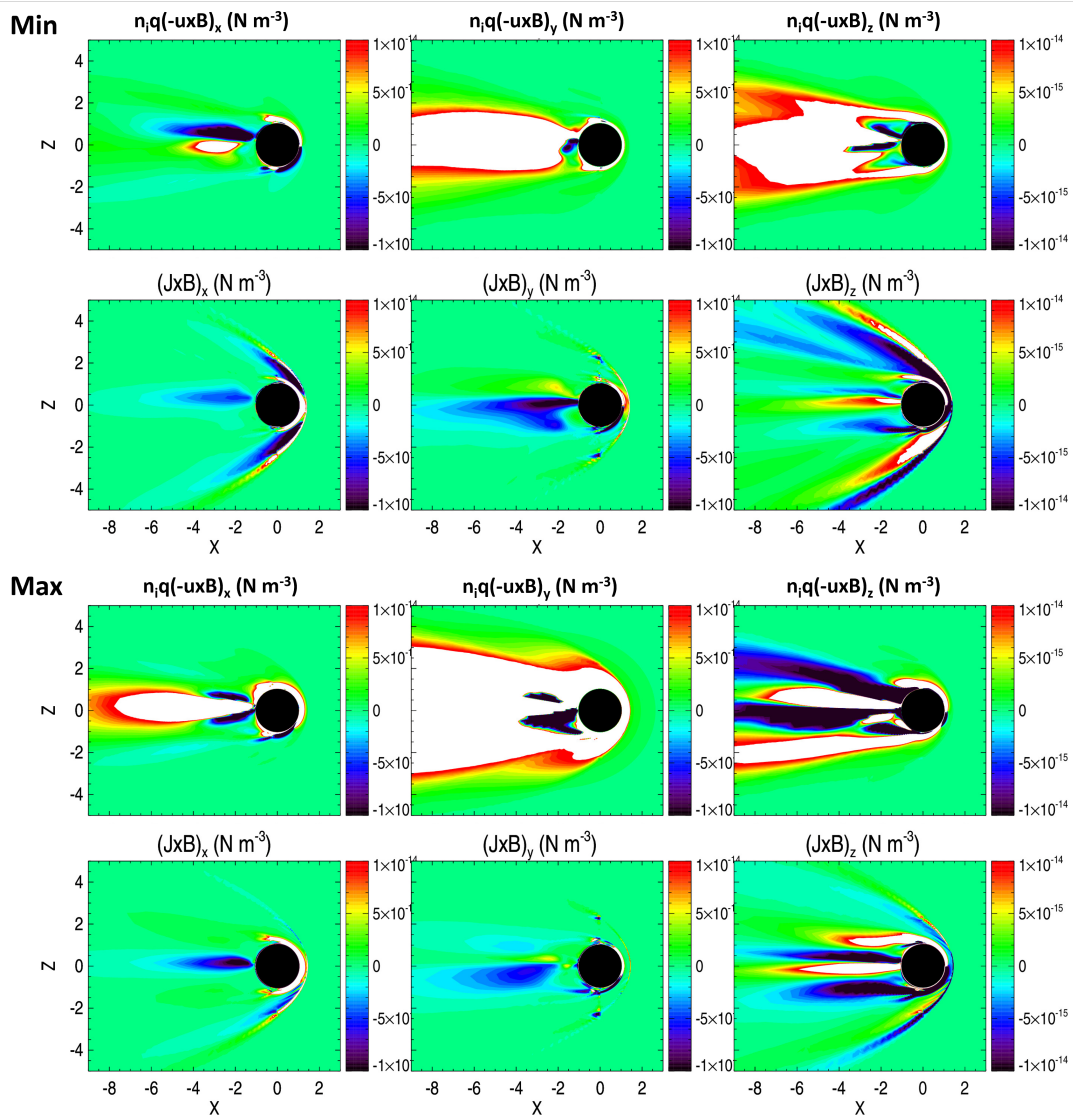

FIGURE 3.4: Color maps of $-\mathbf{u} \times \mathbf{B}$ and $\mathbf{J} \times \mathbf{B}$ forces in the XZ plane. $n_i q$ denotes the total charge density of the three heavy ion species.

Pressure Profile

The pressure profile (Figure 3.5) illustrates the energy transfer in the system. On the dayside, the stellar wind dynamic pressure is converted into thermal pressure at the bow shock (where the blue curve and the red curve cross). The cusp in the total energy curve (black) around the same location is the model's detection of the bow shock, which is purely numerical. Further toward the planet, the thermal pressure is then converted into magnetic pressure, where the magnetic field lines pile up and get deflected around the dayside. The magnetic energy is dissipated across the tail region as the magnetic field diffuses. The remaining energy stored in the magnetotail converts back to thermal and plasma kinetic energy upon magnetotail reconnection, as seen through the rising of the corresponding pressure curves. Although the energy is significantly lower on the nightside, the plasma reaches a terminal dynamic pressure of about 25 nPa for stellar minimum and 70 nPa for stellar maximum. Using the corresponding total ion density, the Maxwell-Boltzmann average kinetic energies of an ion traveling downstream are 1.6 eV (minimum) and 4.4 eV (maximum), both exceeding the average escape energy of 1.2 eV (minimum) and 1.7 eV (maximum) at the pressure balance points (where the green and blue curves intersect).
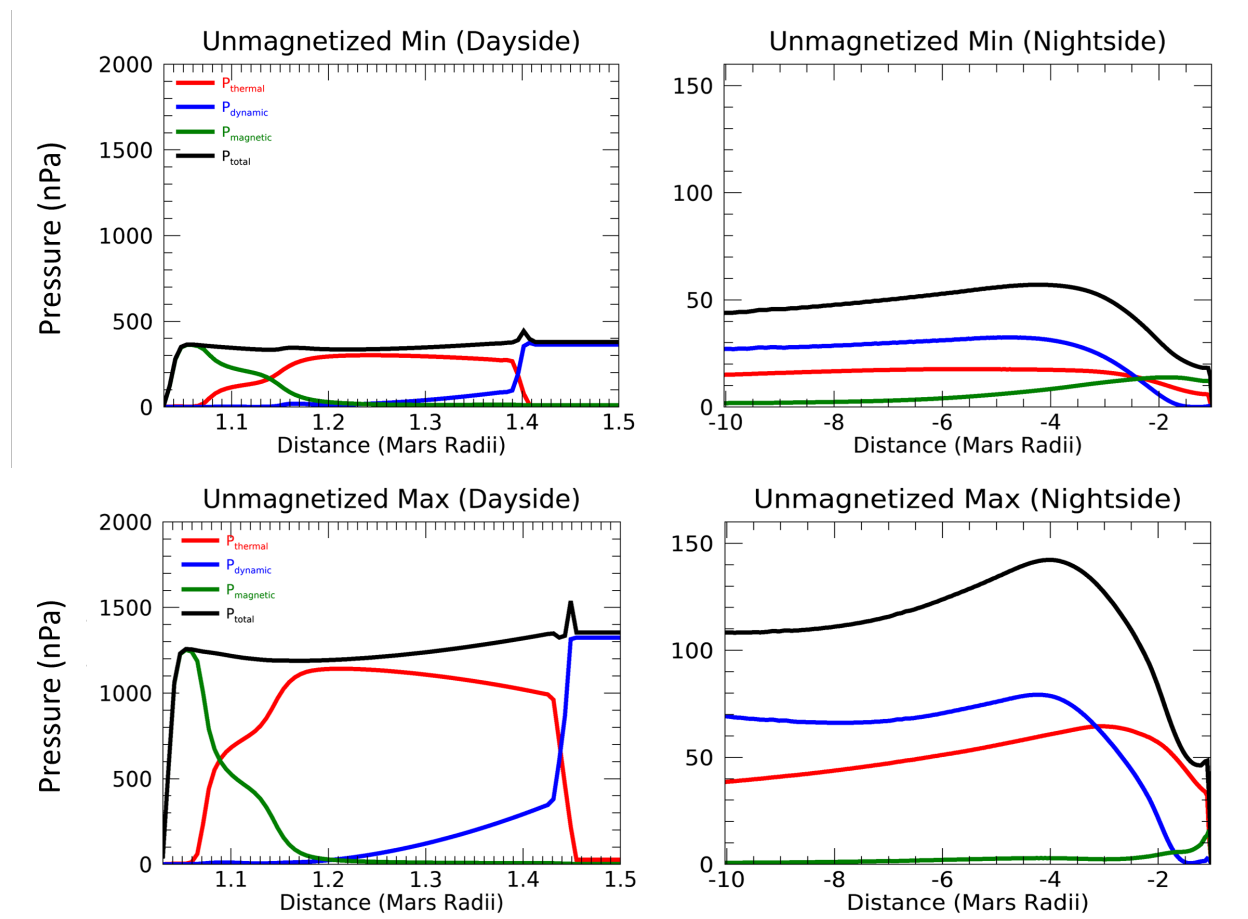
FIGURE 3.5: Pressure profile for an unmagnetized Mars-like exoplanet under stellar minimum and maximum conditions. The dayside pressure is plotted along the substellar line where the stellar rays penetrate the planet at 90 degrees. The nightside pressure is tracked downstream at the same latitude on the opposite side of the planet.

3.1.2 Ion Escape Rates

As a consequence of the stellar wind-planet interaction, we obtained the total escape rates for the major ion species from an unmagnetized and weakly magnetized Mars-like exoplanet, shown in Table 3.1. In the threatening plasma environment at TRAPPIST-1g, the escape rates are about 2 orders of magnitudes higher than the present-day Mars observed by MAVEN [5]. The stellar maximum condition produces an escape rate 4.2 times higher than the stellar minimum. For each case above, O^+ is responsible for almost the entire escape, while CO_2^+ contributes very little. For this reason, although CO_2^+ will still be included in

the total escape rate calculations, Section 3.2 will omit the illustration of its ion density distribution.

Cases	O^+ (s^{-1})	O_2^+	CO_2^+	Total
Unmagnetized Stellar Min	1.33×10^{27}	1.92×10^{25}	1.02×10^{24}	1.35×10^{27}
Unmagnetized Stellar Max	5.59×10^{27}	1.61×10^{25}	2.31×10^{24}	5.61×10^{27}
Crustal Field Stellar Max	5.50×10^{27}	1.65×10^{25}	8.20×10^{23}	5.52×10^{27}

TABLE 3.1: Ion escape rates for the three major ion species. These quantities are the net ion outflow per second at 6 Mars radii.

3.2 Magnetized Mars-like Exoplanet

3.2.1 System Dynamics

This subsection presents the dynamical processes in the system for a Mars-like exoplanet with a non-tilted southward dipole (tilt angle $= 0°$). As Figure 3.6 shows, when an intrinsic dipole field is present, the global magnetosphere increases the interaction area compared to the unmagnetized and crustal field cases. The dipole structure is visible through the closed field lines, as well as its elongation toward the nightside due to stellar wind compression. Two thick magnetotail lobes consisting of stretched open field lines form on the night side, where they meet at the equatorial plane ($z = 0$) to reconnect and create the first current sheet. Above 2 Mars radii to the north, the IMF is perturbed inside the bow shock but points in the same general direction. Near the dayside north pole, the shock alters the IMF direction, where the field lines pile up close to the southern shock. The deflected IMF meets the open field lines returning to the south pole to cause reconnection about 3 planetary radii below the pole, producing the second current sheet.
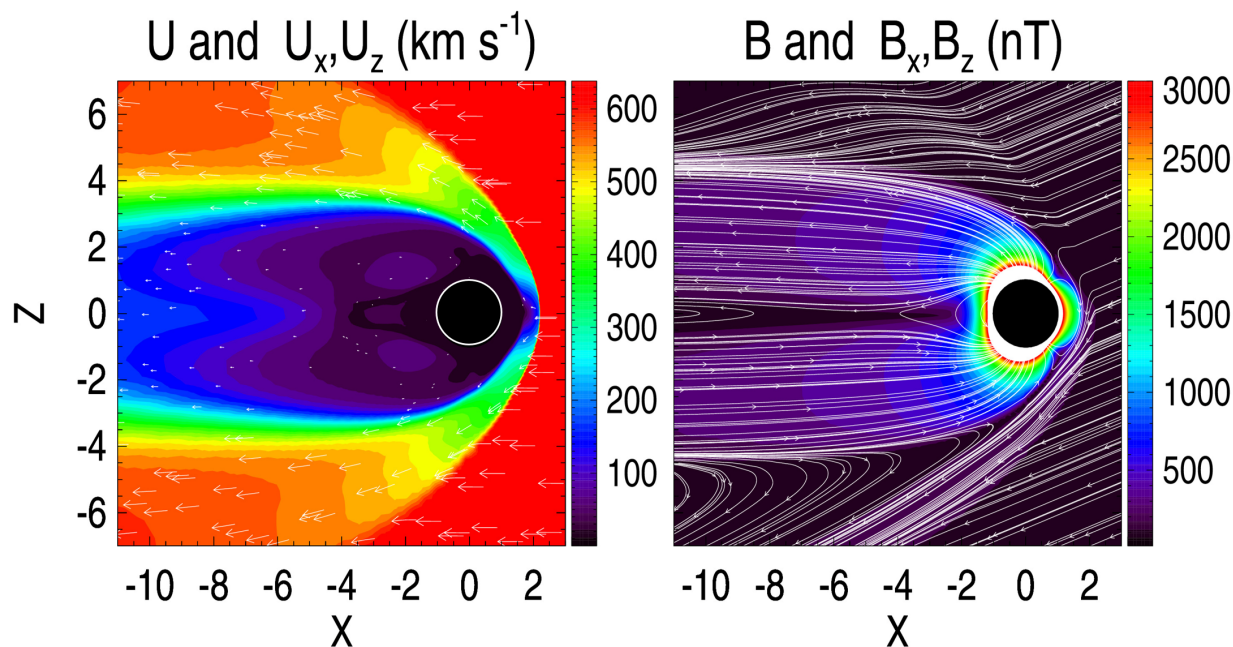
FIGURE 3.6: Plasma velocity and magnetic field around a globally magnetized planet with no dipole tilt (0°). This figure is similar to Figure 3.2 but plotted on a larger spatial range with different color scales.

The pressure profile for a magnetized Mars indicates much higher energy on the dayside. This is due to a fairly strong planetary dipole that provides high magnetic energy. The intrinsic magnetosphere results in a bow shock further away from the planet (2.2 Mars radii). Close to the planet, the total pressure is dominated entirely by magnetic pressure. On the nightside, magnetic pressure drops significantly with distance. It approaches zero close to -4 Mars radii where the dynamic pressure curve starts rising, which is around the magnetotail reconnection site in Figure 3.6. The conversion back to dynamic pressure is very inefficient as the rising blue curve only reaches up to 15 nPa, but this amount of energy is sufficient for escape at -4 Mars radii.
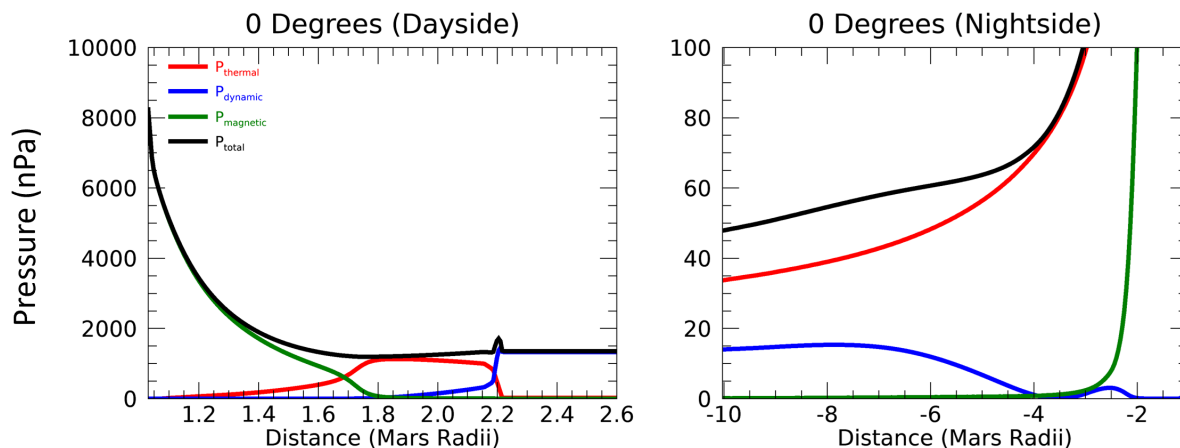
FIGURE 3.7: Pressure profile for a magnetized Mars-like exoplanet with a southward dipole under stellar maximum condition. The plot setting is similar to unmagnetized cases but with different axis scales.

3.2.2   Effect of Dipole Tilt on Ion Loss

The dipole tilt angle determines the magnetic structure, ion density, plasma boundaries, and other properties near the planet, all of which influence the ion loss rate. The following subsections will address variations of these properties caused by changing the tilt angle and highlight the escape rate extremes.

Magnetic Structure and Ion Density Cloud Variation

The magnetic structure and the corresponding ion density at each of the fourteen dipole tilt angles are summarized in Figures 3.8 and 3.9. The topology of the magnetosphere and ion cloud changes substantially with the dipole tilt.

The dayside reconnection pattern undergoes a transition between 30° and 60°. The dipole tilt exceeds a critical point where the IMF starts reconnecting with the forwarded upper magnetospheric dipole. Tracing the field lines at the magnetic north pole, we see that the deflected IMF at the magnetopause meets the opposite-pointing geomagnetic field lines coming out of the pole, resulting in reconnections. Then, the reconnected field lines
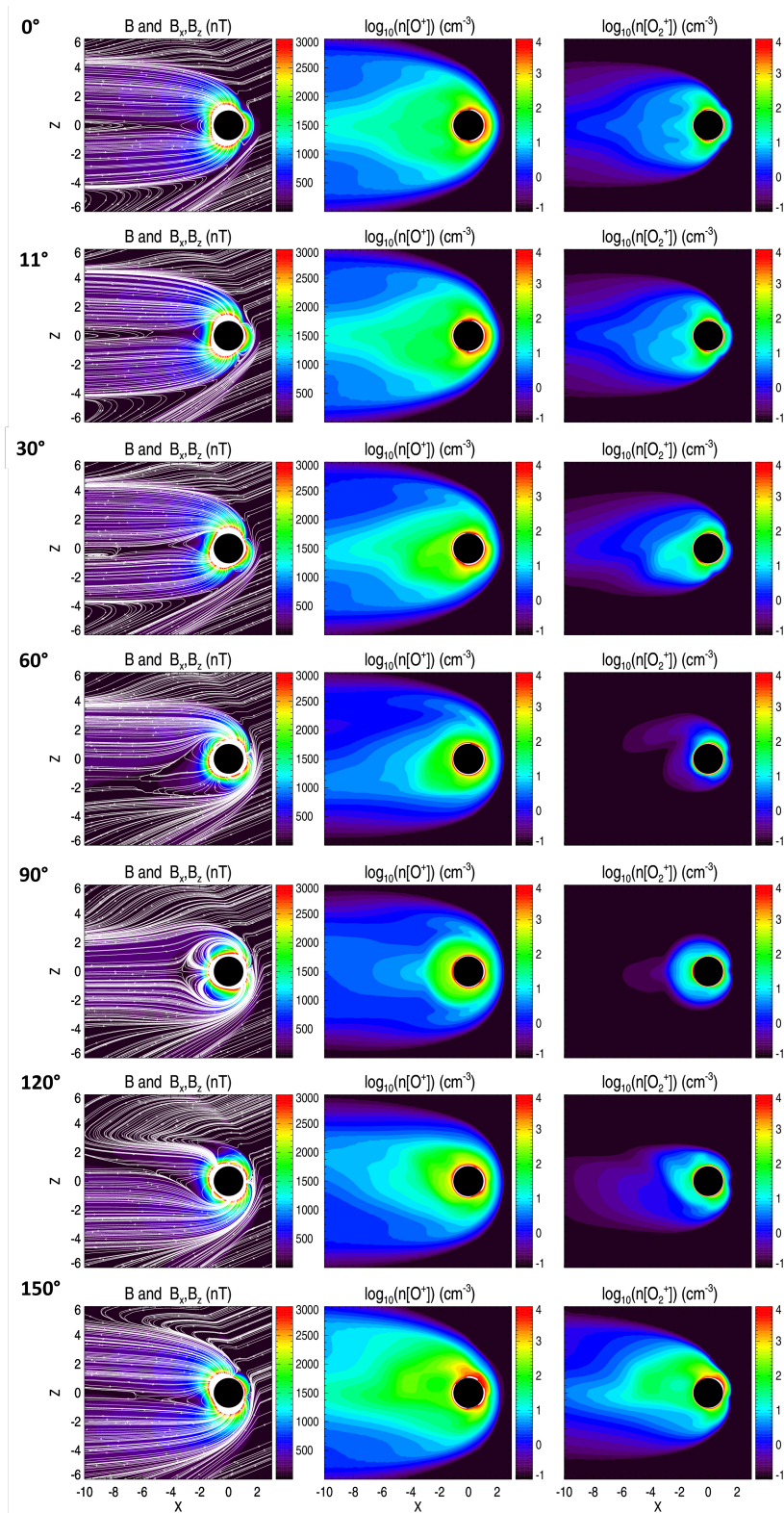
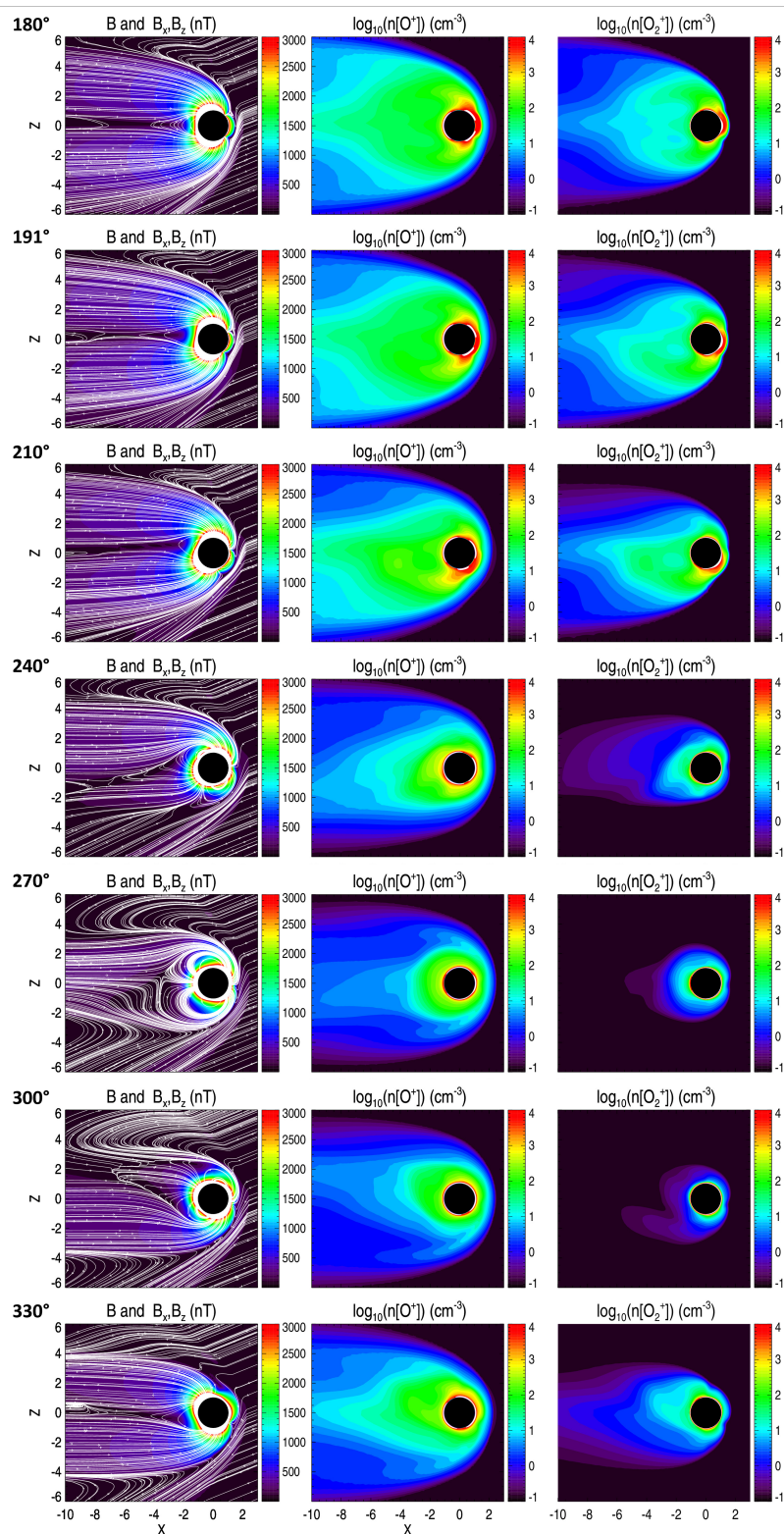FIGURE 3.8: 2-D magnetic structure and ion number density distributions for dipole tilts from 0° to 150°.

FIGURE 3.9: 2-D magnetic structure and ion number density distributions for dipole tilts from 180° to 330°.

reverse downward to drape around the southern magnetosphere. These field lines, and the ones that originate from the same pole but travel upward, form two layers of open field lines all pointing in the -x direction. Hence, no magnetotail reconnection takes place. Unlike the thick magnetotail lobes seen in the 0° and 30° cases, many field lines going out of the magnetic north inside these layers return to the magnetic south. As a result, the 60° case has an elongated closed magnetospheric structure.

Another transition occurs between 90° and 120°. The magnetosphere remains closed at 90°. When the tilt increases to 120°, the south magnetic pole is lifted from the $z = 0$ plane, making the returning geomagnetic field lines more likely to touch and reconnect with the slightly curved anti-sunward IMF. This process creates many open field lines connected to the south magnetic pole. With more reconnections above the geographic north as the dipole continues to lift up, the northern magnetotail lobe fully forms at 150°. The cases from 150° to 210° maintain a magnetic structure with two full tailward lobes. Then, at 240°, the southern lobe starts to break as the magnetic north pole rotates away from the dayside, which reduces the chances of reconnection with the IMF. The overall topology variation is approximately symmetric about 180°. The topology itself on the two sides of 180° appears symmetric about $z = 0$.

The ion density has a negative gradient toward the magnetotail on the nightside. The smallest negative gradient points approximately anti-sunward along the magnetotail near $z = 0$ (within 2 Mars radii in the z direction). The number of ions remains high in this region far down the tail, providing a source of escape. The ion density cloud reflects the magnetospheric structure. A small ($< 30°$) tilt from a vertical dipole (0° or 180°) brings forward one tail lobe and sends back the other. The forwarded lobe counteracts the stellar wind and reduces the density along that lobe. The opposite applies to the lobe being sent back, resulting in a slightly enhanced ion density. For higher tilts from a vertical dipole, one lobe decreases in size while a closed magnetosphere takes shape. The ion density is strengthened in the direction where the closed field lines are elongated.

Ion Escape Rate Variation

The ion distribution varies with the structure inside the magnetosheath, resulting in changes in the escape rate. The upper panel of Figure 3.10 shows the correlation between the ion escape rate and the dipole tilt angle. The tilt adjusts the total escape rate by up to a factor of 4.2, corresponding to a decrease from the unmagnetized case under the same stellar wind condition by a factor between 1.8 and 7.5. The graph is roughly symmetric about an axis between 180° and 191°.

The variations of the two dayside boundaries (bow shock and magnetopause) also depict a symmetry about 180° and 191° with different trends. The net escape rate is approximately inversely proportional to the bow shock location. For the cases with higher escape rates, which correspond to bow shock locations closer to the planet, the stellar wind penetrates further into lower altitudes before slowing down. Hence, the less dominant species, O_2^+, located at lower altitudes are impacted and brought up to higher altitudes, which is consistent with the larger ion clouds in Figure 3.8 for these cases. No clear relation is found between the escape rate and magnetopause location.
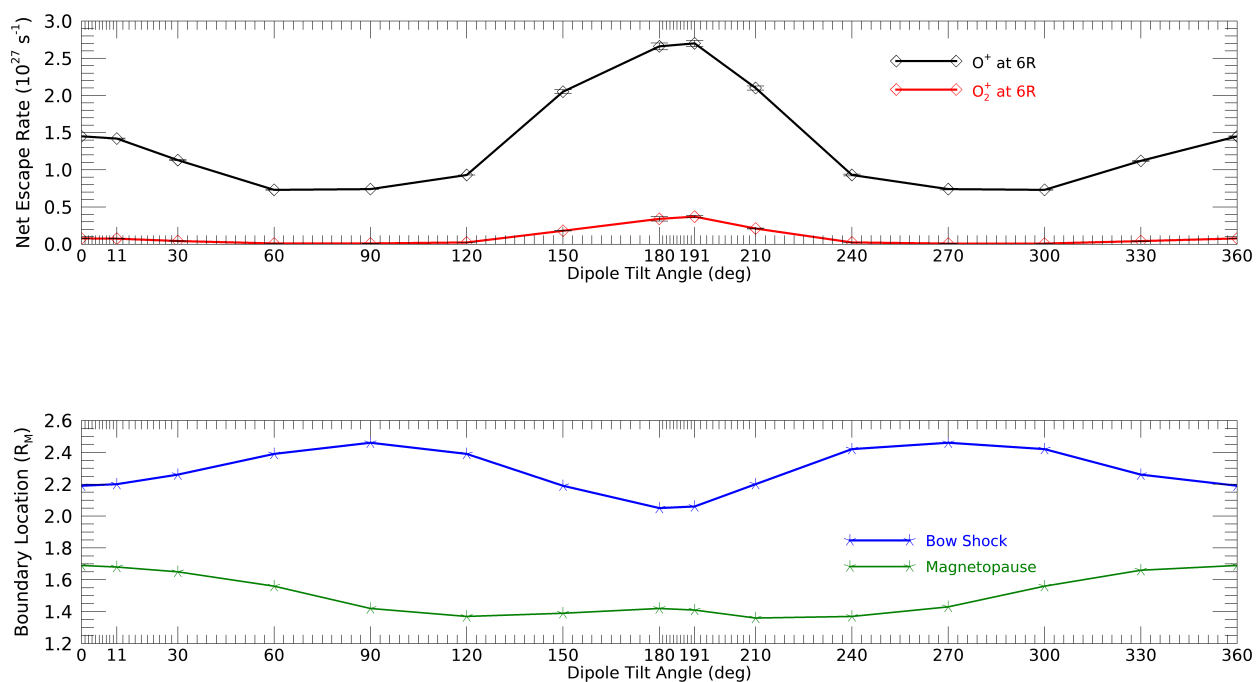
FIGURE 3.10: Relationship between ion escape rate, bow shock location, and dipole tilt angle.

The total escape rate surges from 120° to 150° by over a factor of 2. Symmetrically, it drops by about the same factor from 210° to 240°. In Figure 3.8 and 3.9, the ion density clouds for both species are noticeably larger in the 150° and 210° cases compared to the 120° and 240° cases, especially for O_2^+. In the first panel, reconnection above the south magnetic pole starts at 120°, yet the full upper tailward lobe does not form completely until 150°. In this case, despite the open field lines produced at 120°, they do not direct the ions toward the tail, while at 150°, a large number of ions flow out as the polar wind and travel inside the newborn lobe toward the tail, matching the increased density in the upper region in the second and third panels. Although the magnetic structures of 210° and 240° are symmetric with 150° and 120°, respectively, the formation of the 240° structure from 210° is not exactly the reverse of 150° from 120°. This is likely due to the small -z component of the IMF that causes asymmetry in the magnetosphere.

Minimum and Maximum Escape Rates

Dipole tilts of 60°, 90°, 270°, and 300° lead to minimum ion escape rates. Magnetospheric configuration plays an important role in producing low escape rates. As shown in Figures 3.8 and 3.9, these cases have the most closed magnetospheric structures out of all the magnetized cases. All of them have one magnetic pole not exposed to the stellar wind. The field lines originated from the other pole directly face the stellar wind. They are straightened in the -x direction, creating magnetotail layers draping around the two sides of the planetary magnetosphere. Any reconnections with the IMF occur at the outermost shell of these layers, while the inner field lines remain relatively undisturbed. The innermost geomagnetic field lines are able to stay closed with the shielding of the magnetotail layers. The absence of the magnetotail reconnection due to the parallel field lines further protects the nightside from opening up. While ions escape from the magnetic pole facing the stellar wind, they do so through the outer part of the tail layers. Many of the remaining ions are distributed across the closed field line region, where they are trapped without escaping.

The ion escape rate hits maxima at 180° (3.04×10^{27} s^{-1}) and 191° (3.13×10^{27} s^{-1}). Note that these cases have two opposite-pointing full tail lobes present. Compared to 0° and 11°, 180° and 191° have more open magnetospheres. The dayside of 180° is in favor of reconnection since the geomagnetic field lines near the substellar point (northward) are opposite to the deflected IMF (southward). The opening of the dayside magnetosphere creates a more exposed ionosphere to the stellar wind and thicker magnetotail lobes on the nightside. Similar analysis goes to 11° and 191°. Thus, 180° and 191° cases have larger green regions in their ion clouds. In addition, the red-white regions in the ion contour maps suggest large outflows of O^+ from the poles and O_2^+ from the substellar region, likely a result of exposure to the stellar wind. Both features are not as obvious at 0° and 11°. Consequently, the 180° and 191° cases have about twice the escape rates of 0° and 11° cases.

3.3 Summary

Based on our modeling results, for a Mars-like exoplanet at TRAPPIST-1, the ion escape for all cases is dominated by O^+. For the weakly and unmagnetized cases, the total escape rate is in the order of 10^{27} s^{-1} for stellar minimum and maximum, with the stellar maximum case 4.2 times higher than the stellar minimum case.

For the magnetized cases, the ion escape rate is symmetric about a dipole tilt angle around 180° and 191°, where the escape rate peaks. An enhanced polar wind escape is seen for cases with higher escape rates. Minimum escape rates occur at 60°, 90°, 270°, and 300°, where the dipole is nearly horizontal. Overall, upon lowering the ion loss rate, the dipole tilt regulates the loss rate by up to a factor of 4.

A north or south-ward dipole that is anti-parallel to the IMF usually opens up the magnetosphere. As shown in our results, this is not applicable for radial IMF (IMF with dominant x component). The reconnection pattern is sensitive to the dipole tilt. Reconnection sites depend on which way the IMF is deflected at the dayside magnetopause and the dipole tilt, which determine the direction of the closed field lines at a specific point. A closed magnetosphere still leads to less ion loss, but the way this configuration forms is different.

Chapter 4

Discussion and Implications

An "ideal" dipole for atmospheric retention at near-radial IMF

This study addresses a steady-state environment with an average IMF direction. In reality, the IMF varies based on the stellar cycle and a few other factors, which will change the tilt angle dependence. Given the specific case of a Mars-like exoplanet at TRAPPIST-1g, Our simulation provides insights into a potential IMF-dipole configuration that would lead to a minimum escape rate.

The minimum and maximum stellar wind conditions both suggest an IMF with a large -x component. Despite the variability of IMF, we may assume the predominance of a radial IMF at TRAPPIST-1g. Based on the results, the four cases with minimum escape rates have dipoles that are exactly or nearly horizontal, which are well-aligned or anti-aligned with the IMF. In this case, the upstream stellar wind, IMF, and dipole moment are roughly on the same line. This combination creates relatively closed magnetospheric configurations. This is a result of an unexposed magnetic pole on the nightside and an isolated magnetosphere shielded by open field lines and IMF pointing in the same direction (suppressed reconnection). Therefore, for a magnetized Mars-like exoplanet at TRAPPIST-1g that is frequently exposed to radial IMF, a near-horizontal dipole might be the ideal magnetosphere for atmospheric retention.

Possibility for Habitability

Our model results suggest different fates for a Mars-like exoplanet at TRAPPIST-1g in terms of atmospheric evolution. Despite being in the habitable zone of TRAPPIST-1, such a planet would experience substantial atmospheric loss over a short time scale. However, some specific magnetospheric configurations could still provide a potentially habitable environment. The four cases that yield the minimum escape rates (described in Section 3.2) lead to an atmospheric ion loss rate of around 20.1 kg/s. If the planet starts out with a 0.5-bar atmosphere (similar to ancient Mars), such a loss rate would result in atmospheric retention over gigayear timescales. Given that it takes 0.8 to 1 Gyr for life to form on a planet [20], surface habitability may be possible on a magnetized Mars-like exoplanet with a 5,000 nT near-horizontal dipole. Since this result is determined at stellar maximum, the timescale for atmospheric retention could be further brought up by a few times at less intense stellar wind conditions.

Comparison with a previous study

A 2019 study on ion escape by Dong et al. performed MHD simulations for an Earth-like planet, investigating the role of dipole tilt (obliquity) [9]. Although their upstream stellar wind inputs are similar (stellar maximum at TRAPPIST-1g) to ours, they only kept the x components of the stellar wind velocity and IMF. Their simulation results show minor variations in the total escape rates (up to a factor of 2) for all tilt angles, and all cases yield escape rates in the order of 10^{28} s^{-1}. Our results are different as we obtained total escape rates all in the orders of 10^{26} s^{-1} to 10^{27} s^{-1} and found greater dependence on the dipole tilt angle (a factor of 4). Our escape-tilt correlation also shows a different trend. Namely, for horizontal dipoles (90° and 270°), we acquired minimum escape rates while they acquired maximum.

The qualitative disagreement is illustrated in the differences in the magnetospheric configurations. As described in Chapter 3, our simulations yield closed configurations at 90°

and 270°, and open configurations at 0° and 180°, with 180° more open than 0°. The reverse happens in the Dong et al. (2019) simulations. For a vertical dipole (0° and 180°), there are a large number of closed magnetic field lines on the night side. One might guess that the planetary dipole field strength is causing the difference here. Earth has a strong dipole of around 25,000 nT, resulting in a much thicker magnetosphere than a 5,000 nT dipole. Hence, it is harder to create the two open magnetotail lobes seen in our results. For a horizontal dipole (90° and 270°), instead of open magnetotail field lines shielding a closed magnetosphere, elongated closed field lines form layers at the magnetopause, surrounding a thick lobe of open field lines in the middle. A critical field strength may exist past which the magnetosphere starts to become closed for a vertical dipole and open for a horizontal dipole. The presence of the z-component in the IMF, which causes asymmetry in the magnetosphere, may also play a role in producing the final magnetospheric configurations.

Limitations and future directions

For our multi-species MHD model, the plasma is treated as a single fluid, meaning that the model assumes the same velocity and temperature for ions and electrons. In reality, electrons in this system may have a higher temperature than ions. According to the thermal velocity expression in 3-D, $v_{th} = \sqrt{\frac{8k_BT}{\pi m}}$, higher T for electrons would result in a greater velocity difference with ions. The hot electrons (photoelectrons) increase the scale height of O^+ [7], producing a denser O^+ cloud at higher altitudes and enhancing its escape. If a separate electron pressure equation is solved, the enhanced ambipolar electric field (electron pressure gradient force) can facilitate ion acceleration along open field lines and thus increase the total escape rate. An improved multi-fluid MHD model (called the MFPe model) developed in 2019 by Ma et al. is capable of this task with additional computational resources [17].

Future studies on M dwarf exoplanet atmospheric loss can be improved by more accurately capturing the ambipolar electric field, as mentioned above. Using model simulations, one can explore the role of several variables in the ion loss rate. The Dong 2019 study obtained higher escape rates using a stronger planetary dipole field and a different neutral

atmosphere [9]. It would be worth investigating the escape rate trend over a large range of intrinsic magnetic field strengths and using different atmospheric compositions. Other possible directions include comparing different models and plasma environments for more M dwarf candidates. Potential future space missions like ESCAPE could resolve the EUV spectra of M dwarf stars and the atmospheric content of exoplanets, providing more constraints on the model input.

Chapter 5

Conclusion

Atmospheric retention is crucial for the surface habitability of a planet. Based on the available resources in our galaxy, M dwarf star systems provide the most promising environments possible for life. However, due to the intense radiation and plasma flow from the star, the planet is subject to atmospheric loss over time. Ion escape is a main process of atmospheric loss, where charged particles are produced in the atmosphere through stellar EUV radiation and accelerated by the electric fields in the stellar wind. The magnetospheric structure around the planet plays a key role in the stellar wind-ionosphere interaction, impacting the ion escape rate from the planet.

For this project, we simulated the atmospheric ion loss of a Mars-like exoplanet in the habitable zone of TRAPPIST-1 via a single-fluid multi-species MHD model. We ran a total of 17 cases with different planetary magnetospheric configurations. According to the results, an unmagnetized Mars-like exoplanet has an escape rate in the order of 10^{27}. With a geomagnetic dipole of 5,000 nT at 14 dipole tilt angles, the escape rate is reduced by a factor between 1.8 and 7.5. Under the stellar maximum condition with a relatively radial IMF, our results give minimum escape rates when the dipole is near-horizontal ($\pm 30°$ from the x-axis), and maximum when the dipole is nearly northward (dipole tilt = $180°$ and $191°$). We conclude that in the quasi-radial IMF scenario, a horizontal dipole might be in favor of more closed magnetospheric structures, leading to atmospheric retention over gigayear

timescales and allowing a potentially habitable environment. Future directions point toward the consideration of ambipolar electric fields and examination of other factors including atmospheric content, dipole field strength, and more M dwarf stellar wind inputs.

Bibliography

[1] Acuña, M. H., et al., Magnetic field and plasma observations at mars: Initial results of the mars global surveyor mission, *Science*, *279*(5357), 1676–1680, doi:10.1126/science. 279.5357.1676, 1998.

[2] Akbari, H., L. Andersson, W. K. Peterson, J. Espley, M. Benna, and R. Ergun, Ambipolar electric field in the martian ionosphere: Maven measurements, *Journal of Geophysical Research: Space Physics*, *124*(6), 4518–4524, doi:10.1029/2018JA026325, 2019.

[3] Brain, D., Mars global surveyor measurements of the martian solar wind interaction, *Space Science Rev.*, *126*(12), 77–112, doi:10.1007/s11214-006-9122-x, 2006.

[4] Brain, D. A., F. Bagenal, Y. J. Ma, and G. S. Wieser, Atmospheric escape from unmagnetized bodies, *Journal of Geophysical Research*, *121*(12), 2364–2385, doi: 10.1002/2016JE005162, 2016.

[5] Brain, D. A., et al., The spatial distribution of planetary ion fluxes near mars observed by maven, *Geophysical Research Letter*, *42*(21), 9142–9148, doi:10.1007/ s11214-006-9122-x, 2015.

[6] Cassak, P. A., and Fuselier, Reconnection at earth's dayside magneosphere, in *Astrophysics and Space Science Library*, vol. 427, edited by W. Gonzalez and E. Parker, pp. 213–276, Springer International Publishing Switzerland, doi:10.1007/ 978-3-319-26432-5_6, 2016.

[7] Cohen, O., and A. Glocer, Ambipolar electric field, photoelectrons, and their role in atmospheric escape from hot jupiters, *The Astrophysical Journal Letters*, *753*(1), doi: 10.1002/2016JE005162, 2012.

[8] Dong, C., M. Jin, M. Lingam, V. S. Airapetian, Y. Ma, and B. van der Holst, Atmospheric escape from the trappist-1 planets and implications for habitability, *The Proceedings of the National Academy of Sciences (PNAS)*, *115*(2), 260–265, doi: 10.1073/pnas.1708010115, 2018.

[9] Dong, C., Z. Huang, and M. Lingam, Role of planetary obliquity in regulating atmospheric escape: G-dwarf versus m-dwarf earth-like exoplanets, *The Astrophysical Journal Letters*, *882*(2), doi:10.3847/2041-213/ab372c, 2019.

[10] Dubinin, E., M. Fraenz, M. Pätzold, J. Woch, J. McFadden, and K. F. et al., Impact of martian crustal magnetic field on the ion escape, *Journal of Geophysical Research: Space Physics*, *125*(10), doi:10.1029/2020JA028010, 2020.

[11] Fowler, C. M., K. G. Hanley, J. McFadden, J. Halekas, S. J. Schwartz, and C. M. et al., A maven case study of radial imf at mars: Impacts on the dayside ionosphere, *Journal of Geophysical Research: Space Physics*, *127*(12), doi:10.1029/2022JA030726, 2022.

[12] Gunell, H., R. Maggiolo, H. Nilsson, G. S. Wieser, R. Slapak, J. Lindkvist, M. Hamrin, and J. D. Keyser, Why an intrinsic magnetic field does not protect a planet against atmospheric escape, *Astronomy & Astrophysics*, *614*(3), doi:10.1051/0004-6361/201832934, 2018.

[13] Kopparapu, R. K., et al., Habitable zones around main-sequence stars: New estimates, *The Astrophysical Journal*, *765*(2), doi:10.1088/0004-637X/765/2/131, 2013.

[14] Lavraud, B., J. E. Borovsky, A. J. Ridley, E. W. Pogue, M. F. Thomsen, H. Rème, A. N. Fazakerley, and E. A. Lucek, Strong bulk plasma acceleration in earth's magnetosheath: A magnetic slingshot effect?, *Geophysical Research Letters*, *34*(14), doi:10.1029/2007GL030024, 2007.

[15] Ma, Y., A. F. Nagy, I. V. Sokolov, and K. C. Hansen, Three-dimensional, multispecies, high spatial resolution mhd studies of the solar wind interaction with mars, *Journal of Geophysical Research: Space Physics*, *109*(211), doi:10.1029/2003JA010367, 2004.

[16] Ma, Y., C. Russell, R. Strangeway, G. Toth, A. Nagy, and D. Brain, How does the planetary magnetic field impact on ion escape rate?, PowerPoint Presentation, 2020.

[17] Ma, Y., et al., Importance of ambipolar electric field in driving ion loss from mars: Results from a multifluid mhd model with the electron pressure equation included, *Journal of Geophysical Research: Space Physics*, *124*(11), 9040–9057, doi:10.1029/2019JA027091, 2019.

[18] Peacock, S., T. Barman, E. L. Shkolnik, P. H. Hauschildt, and E. Baron, Predicting the extreme ultraviolet radiation environment of exoplanets around low-mass stars: The trappist-1 system, *The Astrophysical Journal*, *871*(2), doi:10.3847/1538-4357/aaf891, 2019.

[19] Schunk, R., and A. Nagy, *Ionospheres–Physics, Plasma Physics, and Chemistry*, 2nd ed., Cambridge University Press, Cambridge, UK, 2009.

[20] Shields, A. L., S. Ballard, and J. A. Johnson, The habitability of planets orbiting m-dwarf stars, *Physics Reports*, *663*, 1–38, doi:10.1016/j.physrep.2016.10.003, 2016.

[21] Terada, N., H. Shinagawa, T. Tanaka, K. Murawski, and K. Terada, A three-dimensional, multispecies, comprehensive mhd model of the solar wind interaction with the planet venus, *Journal of Geophysical Research: Space Physics*, *114*, doi:10.1029/2008JA013937, 2009.

[22] Yau, A. W., T. Abe, M. André, and W. K. P. Andrew D. Howarth, Ionospheric ion acceleration and transport, in *Magnetospheres in the Solar System*, vol. N/A, edited by R. Maggiolo, N. André, H. Hasegawa, D. T. Welling, Y. Zhang, and L. J. Paxton, pp. 207–217, American Geophysical Union, Washington, DC, US, doi: 10.1002/9781119815624, 2021.